Title
Electronic structure of $LuRh_2Si_2$: 'small' Fermi surface reference to $YbRh_2Si_2$

Journal
New Journal of Physics, 15(9)

ISSN
1367-2630

Authors
Friedemann, Sven
Goh, Swee K
Rourke, Patrick M C
et al.

Publication Date
2013-09-10

DOI
10.1088/1367-2630/15/9/093014

New Journal of Physics
The open access journal for physics

Electronic structure of $LuRh_2Si_2$: 'small' Fermi surface reference to $YbRh_2Si_2$

Sven Friedemann[1,4], Swee K Goh[1], Patrick M C Rourke[1,5], Pascal Reiss[1], Michael L Sutherland[1], F Malte Grosche[1], Gertrud Zwicknagl[2] and Zachary Fisk[3]

[1] Cavendish Laboratory, University of Cambridge, JJ Thomson Avenue, CB3 0HE Cambridge, UK
[2] Institute for Mathematical Physics, TU Braunschweig, Mendelssohnstraße 3, D-38106 Braunschweig, Germany
[3] Department of Physics and Astronomy, University of California, Irvine, CA 92697-4575, USA
E-mail: sf425@cam.ac.uk

New Journal of Physics **15** (2013) 093014 (24pp)
Received 29 March 2013
Published 10 September 2013
Online at http://www.njp.org/
doi:10.1088/1367-2630/15/9/093014

Abstract. We present band structure calculations and quantum oscillation measurements on $LuRh_2Si_2$, which is an ideal reference to the intensively studied quantum critical heavy-fermion system $YbRh_2Si_2$. Our band structure calculations show a strong sensitivity of the Fermi surface on the position of the silicon atoms z_{Si} within the unit cell. Single crystal structure refinement and comparison of predicted and observed quantum oscillation frequencies and masses yield $z_{Si} = 0.379\,c$ in good agreement with numerical lattice relaxation.

This value of z_{Si} is suggested for future band structure calculations on $LuRh_2Si_2$ and $YbRh_2Si_2$. $LuRh_2Si_2$ with a full f electron shell represents the 'small' Fermi surface configuration of $YbRh_2Si_2$. Our experimentally and *ab intio* derived quantum oscillation frequencies of $LuRh_2Si_2$ differ significantly from the results of earlier measurements on $YbRh_2Si_2$. Consequently, our results confirm the contribution of the f electrons to the Fermi surface of $YbRh_2Si_2$ at

[4] Author to whom any correspondence should be addressed.
[5] Current address: National Research Council Canada, 1200 Montreal Road, Ottawa, Ontario K1A 0R6, Canada.

high magnetic fields. Yet, the limited agreement with refined fully itinerant local density approximation calculations highlights the need for more elaborate models to describe the Fermi surface of $YbRh_2Si_2$.

Contents

1. Introduction

$LuRh_2Si_2$ is an intermetallic compound crystallizing in the tetragonal $ThCr_2Si_2$ structure shared by a variety of compounds including some of the recently discovered pnictide superconductors like $BaFe_2As_2$ [1] and heavy fermion materials like $CeCu_2Si_2$ [2]. In particular, it is isostructural to the heavy fermion material $YbRh_2Si_2$ with almost identical lattice parameters (cf table 1). Moreover, $LuRh_2Si_2$ has the same electronic configuration as $YbRh_2Si_2$ except that $LuRh_2Si_2$ has a completely filled 4f electron shell whereas in $YbRh_2Si_2$ the trivalent configuration of Yb has one electron missing in the 4f shell. This missing electron can be regarded as a 4f hole. In analogy to the Ce based heavy fermion systems with one electron in the 4f shell, the hole in the 4f shell of $YbRh_2Si_2$ is the basis for the rich physics of this system. The scattering of conduction electrons from the 4f hole—known as the Kondo effect—gives rise to new states near the Fermi energy which can be regarded as composite quasiparticles formed of the f hole and the conduction electrons. These quasiparticles carry the same quantum numbers as non-interacting electrons, however, they posses highly renormalized properties like a hugely enhanced mass. This can for instance be seen in the three orders of magnitude difference in the Sommerfeld coefficient exceeding $1\,J\,mol^{-1}\,K^{-1}$ for $YbRh_2Si_2$ in the field induced Fermi liquid state compared to few $mJ\,mol^{-1}\,K^{-1}$ for $LuRh_2Si_2$ [3, 4]. At temperatures below $T_N = 70\,mK$, $YbRh_2Si_2$ undergoes a transition into an antiferromagnetically ordered state which can be fully suppressed with a small critical field of 60 mT (for fields in the basal plane) [5]. At zero temperature the transition from this magnetically ordered state to the paramagnetic state represents a quantum critical point (QCP). $YbRh_2Si_2$ has emerged as a prototypical system for a new class of QCPs which need descriptions beyond the order parameter notion [6]. Hall effect measurements show a crossover in the Hall coefficient which sharpens to a jump at the QCP in the extrapolation to zero temperature [7, 8]. This points towards a sudden reconstruction

Table 1. Lattice parameters of $LuRh_2Si_2$ were obtained at room temperature from x-ray diffraction measurements of powdered single crystals [10]. The Wyckoff positions z_{Si} were deduced from single crystalline structure refinement [11]. For $YbRh_2Si_2$ the height of the unit cell, c, has been reported to depend on the exact Rh content [12] whereas no change in the z_{Si} parameter was resolved [11, 13]. So far no indications for variations in the Rh content or c have been reported for $LuRh_2Si_2$.

Compound	a, b (Å)	c (Å)	z_{Si} (c)
$LuRh_2Si_2$	4.006(1)	9.838(3)	0.379(2)
$YbRh_2Si_2$	4.007(1)	9.858 – 9.862	0.379(2)

of the Fermi surface which is not expected at a QCP where the magnetic order parameter evolves continuously. Rather, these results suggest the breakdown of the Kondo effect and the disintegration of the composite quasiparticles. Within this scenario, the Fermi surface evolves from 'large', including the f electron states in the paramagnetic phase, to 'small' in the magnetic phase formed of the non-f states only. The latter configuration is paralleled by $LuRh_2Si_2$ as here the completely filled f states lie well below the Fermi energy and do not contribute to the Fermi surface. In fact, when tuning across the QCP towards the suggested 'small' Fermi surface configuration, i.e. from large fields to low fields, the Hall coefficient crossover in $YbRh_2Si_2$ has a trend towards the Hall coefficient of $LuRh_2Si_2$ with its value increasing in the direction of the even larger value observed in $LuRh_2Si_2$ [4]. Interestingly, chemical pressure appears to lead to a detaching of the Fermi surface reconstruction from the antiferromagnetic QCP [9]. This underpins the importance to understand the electronic structure of this prototypical quantum critical material.

Moreover, at a magnetic field $\mu_0 H_0 \approx 10\,\mathrm{T}$ a second transition is observed in transport, thermodynamic and quantum oscillation measurements on $YbRh_2Si_2$ [14, 15]. With the Kondo temperature and H_0 representing similar energy scales and exhibiting scalable pressure dependences, one might associate H_0 with the polarization of the Kondo singlet states and a suppression of the Kondo effect, yielding again a 'small' Fermi surface above H_0 [16]. However, the continuous evolution of the quantum oscillation frequencies at H_0 rather indicates a complete depopulation of one Fermi surface branch. This field dependence is a strong indicator for the 'large' Fermi surface character as this is not expected for a system with localized f electrons. In fact, renormalized band structure calculations suggest nonlinear dependences of the Fermi surface cross sections in magnetic field [17] which lead to changing frequencies in quantum oscillation measurements. However, the comparison of measured angular dependences in $YbRh_2Si_2$ with local density approximation (LDA) calculations of both $LuRh_2Si_2$ and $YbRh_2Si_2$ representing the 'small' and 'large' Fermi surface, respectively, were inconclusive [15, 18]. While LDA is known to fall short of modelling Yb-based heavy fermion systems [19], LDA has proved reliable for normal metals such as $LuRh_2Si_2$. The discrepancies between the frequencies observed in $YbRh_2Si_2$ and those expected from the calculated 'small' Fermi surface argue for a large Fermi surface scenario in $YbRh_2Si_2$ at high magnetic fields. Moreover, the lack of agreement between the measured frequencies and those expected from LDA calculations within a 'large' Fermi surface scenario may be attributed to the known shortcomings of LDA calculations in Yb-based heavy fermion materials. All these earlier

calculations [15, 18, 20] were based on generic lattice parameters different from the refined values obtained in the present study.

For many systems of the $ThCr_2Si_2$ structure there is a strong sensitivity of the electronic structure to the precise crystal structure. In particular, the Wyckoff parameter specifying the position z_{Si} of the Si atoms has a large influence on the band structure as demonstrated for $CeRu_2Si_2$ and $LaRu_2Si_2$ [21]. For $LaRu_2Si_2$ a lattice relaxation yielded a value z_{Si} far from the experimental value and, moreover, led to a Fermi surface topology in much better agreement with quantum oscillation measurements. In the iron pnictides, the Fe–As–Fe angle which is an equivalent measure of the same Wyckoff parameter z_{Si} is crucial for the nesting of the Fermi surface sheets and for the optimum superconducting transition temperature [1, 22]. These findings for other members of the $ThCr_2Si_2$ structure family underpin the need to precisely determine the Si position for $LuRh_2Si_2$ and $YbRh_2Si_2$ and its significance for their electronic structure. Previous electronic band structure calculations on $LuRh_2Si_2$ and $YbRh_2Si_2$ used either a generic value $z_{Si} = 0.375\,c$, reflecting highest local symmetry, while other band structure studies did not reveal the value used [4, 15, 18, 20, 23, 24]. For $LuRh_2Si_2$, also, a strong dependence of the Fermi surface topology with respect to z_{Si} has been found in a comprehensive band structure calculation [25]. This confirms the need to use the precisely determined z_{Si} rather than the generic value for the structure type [26].

Here, we present a detailed study of the electronic structure of $LuRh_2Si_2$ using Shubnikov–de Haas measurements which we compare with band structure calculations. Best agreement between predicted and observed quantum oscillation frequencies is obtained at the precisely determined experimental value $z_{Si} = 0.379\,c$. Future electronic structure calculations should use the experimental Wyckoff parameter z_{Si} and precisely determined lattice parameters. Our electronic structure investigations on $LuRh_2Si_2$ provide a more accurate reference for the 'small' Fermi surface configuration. In fact, significant modifications arise from the corrected silicon position z_{Si}. Nevertheless, we find even stronger differences between the experimental results on $YbRh_2Si_2$ and our refined 'small' Fermi surface calculations.

In addition, we find indications that some of the quantum oscillations in $YbRh_2Si_2$ with frequencies between 4 and 7 kT arise from harmonics. If this proves to be right, band structure calculations may be compared to the remaining frequencies below 4 kT and above 7 kT, only. We suggest further experiments to investigate this hypothesis.

Finally, our combined band structure and Shubnikov–de Haas study identifies two bands and thus supports the application of the two-band model to describe the Hall effect in $LuRh_2Si_2$ and $YbRh_2Si_2$ [4]. The comprehensive knowledge on the band structure of $LuRh_2Si_2$ obtained here is the basis for a full understanding of the complex transport properties of $LuRh_2Si_2$.

2. Band structure calculations

2.1. Computational details

Very accurate powder x-ray diffraction measurements and single crystal structure refinement were performed on a piece of the same single crystal used for the Shubnikov–de Haas-measurements. The obtained crystallographic parameters of the tetragonal unit cell with space group $I4/mmm$ (# 139) as given in table 1 with the relative atomic positions Lu (0,0,0), Rh (0,1/2,1/4) and Si (0,0,z_{Si}) were used for the band structure calculations. We show below a very good agreement between quantum oscillation frequencies observed at low temperature and

those calculated on the basis of the crystallographic parameters measured at room temperature. This suggests that the crystallographic parameters are the same at low temperature. The band structure and the Fermi surface topology are found to be very sensitive to details of the crystal structure, particularly the position of the Si atoms z_{Si} [25]. For this reason, we calculate the variation with z_{Si} of the total energy.

We use the WIEN2k density functional theory code to perform band structure calculations [27]. Band energies were calculated on a 800 000 k-point mesh in the first Brillouin zone using the Perdew–Burke–Ernzerhof generalized gradient approximation to the exchange-correlation potential [28], $RK_{max} = 7$, and an energy range -6 to 5 Ry. This corresponds to a valence band treatment of 4f, 5s, 5p, 5d and 6s electrons for Lu, 4p, 4d and 5s for Rh, and 3s and 3p for Si. WIEN2k is based on a full potential augmented plane wave and local orbits approach [27]. Relativistic effects and spin–orbit coupling are included on a one-electron level with relativistic local orbits used for Lu and Rh whereas Si is well approximated by non-relativistic local orbitals due to its light mass. The density of states (DOS) was calculated utilizing the tetrahedron method. Fermi surfaces are visualized with the XCrySDen program [29]. Extremal orbits and effective masses were calculated using the SKEAF algorithm [30] at an interpolation of 350 in the full Brillouin zone which corresponds to an interpolation factor of ≈5 with respect to the k-mesh of the band structure calculations. This allows to accurately detect frequencies down to 0.017 kT. The usage of a super cell yields reliable results for orbits extending beyond the first Brillouin zone which is particularly relevant for the comparison with high frequency oscillations in $LuRh_2Si_2$ and $YbRh_2Si_2$.

2.2. *Electronic structure and Fermi surface*

We start by optimizing the crystal structure with respect to the Si position z_{Si} by minimizing the total energy obtained from our band structure calculations whilst keeping the lattice parameters a and c fixed at their precisely determined experimental values (cf table 1). As can be seen from figure 1 the total energy is minimal for $z_{Si} = 0.381\,c$. This value agrees with that obtained from crystal structure refinement $z_{Si} = 0.379(2)\,c$ within experimental accuracy [11]. Moreover, the energy difference between the experimental and relaxed Si position amounts to ≈10 meV (≈100 K) only. Indeed as we shall see from the comparison of calculated orbits with experimentally observed quantum oscillation frequencies, we find best agreement for the experimental z_{Si} (cf [25]). In the following we present results obtained for the experimentally determined value $z_{Si} = 0.379\,c$, if not stated otherwise.

We now turn to the DOS as displayed in figure 2. Most prominently, the large DOS peaks well below the Fermi energy at -6 and -4 eV arise from the Lu 4f states, in good agreement with expected behaviour for a completely filled f shell with small radial extension. The Rh d states originating from the large overlap of Rh orbitals within the Rh–Si layers (cf crystal structure in inset of figure 1) are distributed over a large energy range and dominate the DOS at the Fermi energy. A minor contribution arises from the Si states as part of the Rh–Si layers. Yet, the admixture of the Si states within this layer causes the sensitivity to the Si position, as will be discussed below [25]. The Si s states lie far below the Fermi energy at about -10 eV. The total DOS at the Fermi energy amounts to 2.4 states per eV and unit cell which is slightly higher than reported previously (based on a different z_{Si}) [4], corresponding to a Sommerfeld coefficient $\gamma \approx 5.7\,\mathrm{mJ\,K^{-2}\,mol^{-1}}$ in good agreement with the value of $\gamma \approx 6.5\,\mathrm{mJ\,K^{-2}\,mol^{-1}}$ found experimentally [4].

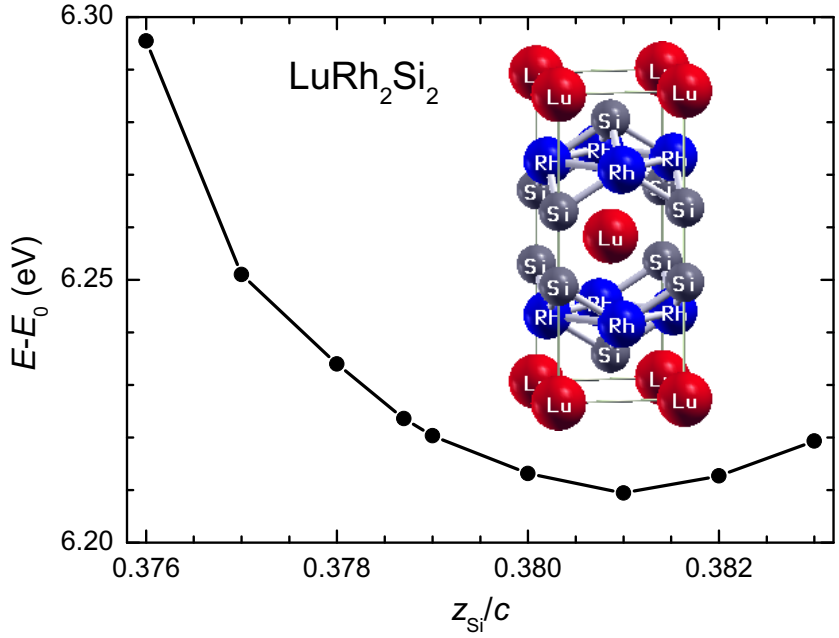

Figure 1. Total energy of $LuRh_2Si_2$ in our bandstructure calculations as a function of z_{Si}. A constant offset of $E_0 = -673$ keV has been subtracted. The inset depicts the crystal structure.

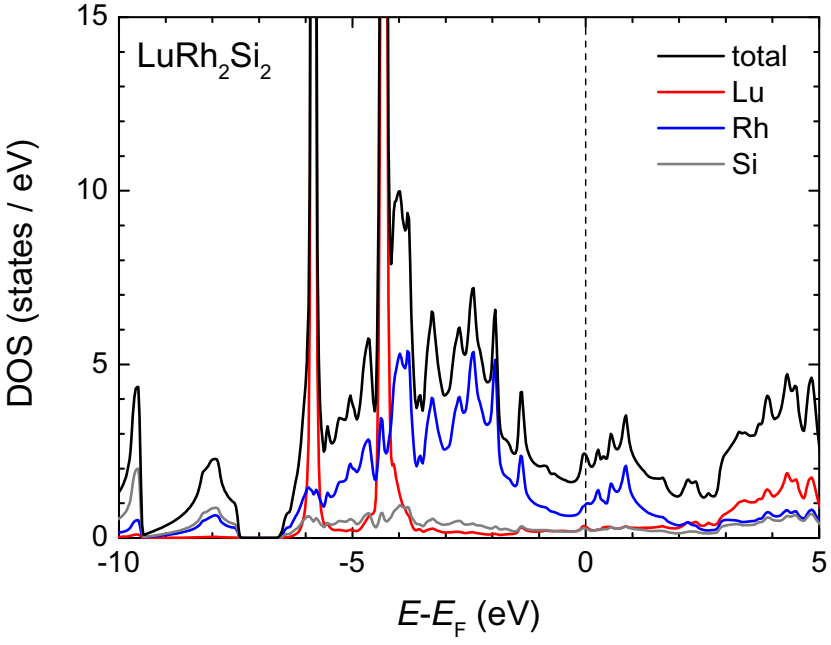

Figure 2. DOS plotted against energy with the Fermi energy E_F as reference. Colours represent the band character; at the Fermi energy Rh 4d states dominate.

The electronic band structure is shown in figure 3. In general, we find good agreement with previously reported band structure calculations on $LuRh_2Si_2$ and on the 'small' Fermi surface (f-core) configuration of $YbRh_2Si_2$. Small differences in the vicinity of the Fermi energy of our

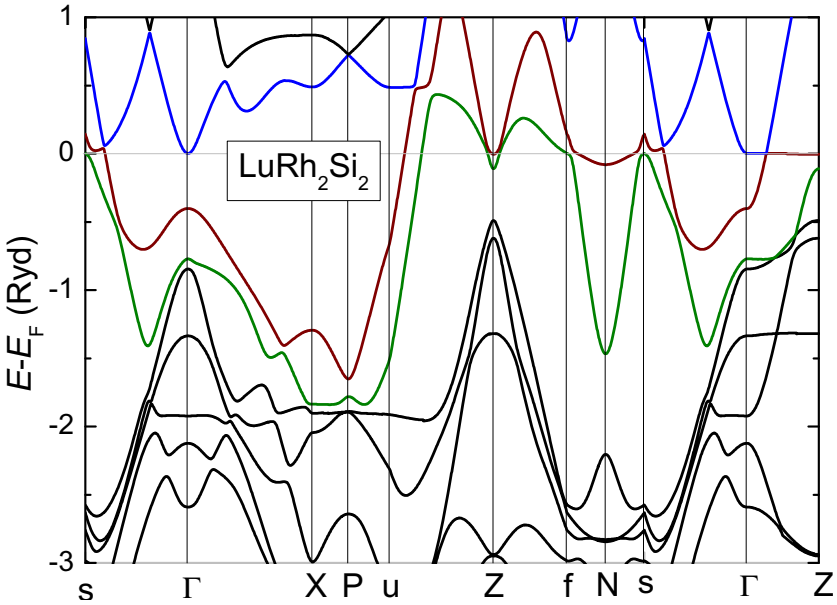

Figure 3. Band structure of $LuRh_2Si_2$ for $z_{Si} = 0.379\,c$ along symmetry lines with the Fermi energy $E_F = 0$ as the reference energy. The conventional notation is adopted with $Z(0,0,1)$, $\Gamma(0,0,0)$, $X(1,1,0)$, $P(1,1,1)$ and $N(1,0,1/2)$ in units of $(\pi/2a, \pi/2a, \pi/2c)$. The labels s, f and u refer to $(\tilde{a},0,0)$, $(\tilde{b},0,1)$ and $(\tilde{b}, \tilde{b}, 1)$, respectively, with $\tilde{a} = 1 + (a/2c)^2$ and $\tilde{b} = 1 - (a/2c)^2$. Bands close to the Fermi energy are represented in colour.

band structure calculations with respect to previous studies are due to the strong sensitivity to the Si position [4, 15, 23, 24]. For $YbRh_2Si_2$ a variation of the crystallographic c-axis has been identified to originate from minute variations in the Rh content. For $LuRh_2Si_2$ no variations in the Rh content or c are reported so far. Moreover, similar changes in the c parameter as for $YbRh_2Si_2$ do not yield significant changes in the band structure of $LuRh_2Si_2$.

As discussed above, most of the bands have dominantly Rh 4d character. Around the Z point the Si $3p_z$ states admix strongly, and this causes the sensitivity of the band structure to z_{Si} [25]. Changes in the Si position change the penetration of the Si p_z orbitals into the Rh $d_{x^2-y^2}$ orbitals within the Rh layers. This causes a shift of the bands at the Fermi energy around the Z point as detailed in [25]. As a consequence, the character of the band intersecting the Fermi energy changes from Rh $d_{x^2-y^2}$ like at low z_{Si} to Si p_z like at $z_{Si} \geqslant 0.379\,c$. The mass of the bands associated with the Rh $d_{x^2-y^2}$ and the Si p_z states differ significantly, as can be seen from the stronger curvature of the upper band. This will serve as an important point in comparison with experimental data below.

Three bands are close to the Fermi energy (cf coloured bands in figure 3). For $z_{Si} = 0.379\,c$, however, only the two at lower energy (green and red) cross the Fermi energy. These two bands give rise to the Fermi surface sheets shown in figure 4, nicely resembling previous calculations [4, 15, 23, 31]. They consist of two Z-centred surfaces, a closed doughnut shaped D sheet and a J sheet (previously dubbed 'jungle gym'), with the latter one extending across the Brillouin zone boundary, connected via tubes along the $a^\star$ direction.

The main differences to previous band structure calculations arise due to the corrected Si position of our band structure calculations [25]: We do not obtain a third pillbox shaped P sheet.

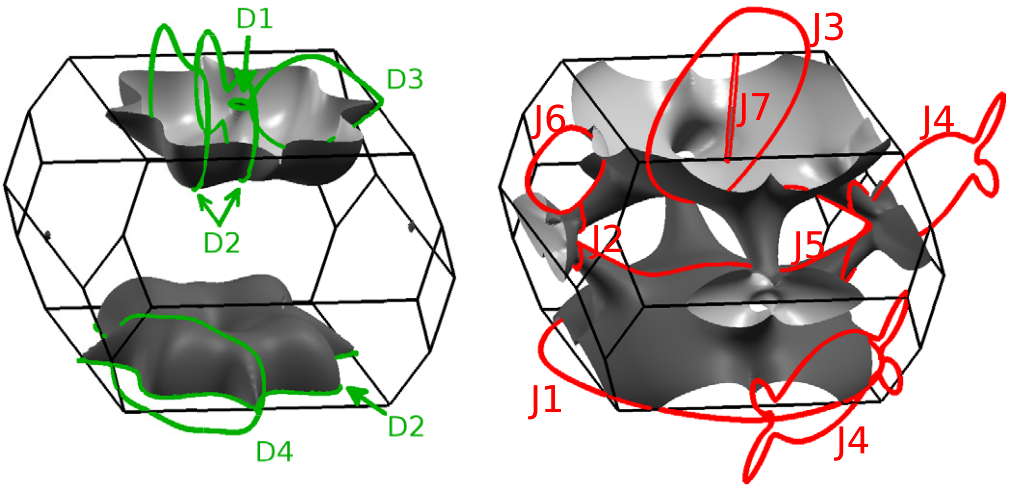

Figure 4. Calculated Fermi surfaces: a doughnut shaped D sheet and a interconnected 'jungle gym' J sheet were obtained using the experimental value for the Si position $z_{\mathrm{Si}} = 0.379\,c$. Green and red lines represent selected extremal orbits.

This can be seen from the band structure plot in which the band associated with the pillbox (blue in figure 3) remains slightly above the Fermi energy at the Γ point. This P band is only populated for $z_{\mathrm{Si}} \leqslant 0.378\,c$. At $z_{\mathrm{Si}} = 0.379\,c$, we find a very thin central pillar in the J sheet (encircled by orbit J7 figure 4) which arises from a hybridization with the states forming the P band. The fact that the pillar is present but the P sheet is absent is due to a small gradient in the dispersion relation from the Γ point to the Z point as detailed in [25]. In fact, the pillar is disconnected from the main sheet due to this gradient, as can be seen in figure 4 (orbit J7).

The hole in the D sheet persists even for large variations of the Si position z_{Si} as shown in [25]. This hole is associated with the band crossing the Fermi energy around the Z point. It is minimal in size for $z_{\mathrm{Si}} = 0.379\,c$ and widens for both decreasing and increasing z_{Si}. The character of the hole in the D sheet, however, changes from Rh $\mathrm{d}_{x^2-y^2}$ at $z_{\mathrm{Si}} \lesssim 0.378\,c$ to Si p_z for $z_{\mathrm{Si}} \gtrsim 0.379\,c$. This is accompanied by a change in the mass of this orbit as mentioned above. The steep curvature of the Si p_z-like band corresponds to a lower mass than the flat Rh $\mathrm{d}_{x^2-y^2}$ band. We shall use these sensitivities of the Fermi surface topology and the masses of extremal orbits for a detailed comparison with the observed quantum oscillations below.

3. Shubnikov–de Haas measurements

3.1. Experimental details

Single crystal samples of $LuRh_2Si_2$ were grown in indium flux as described earlier [32]. Shubnikov–de Haas oscillations on a bar shaped sample were measured using a standard four probe resistivity measurement. Contacts were provided by 25 μm gold wires spot welded to the sample of dimensions of approximately $20 \times 100 \times 2000\,\mu\mathrm{m}^3$. The current was applied within the basal plane at an angle of $\approx 10^\circ$ from the (100) axis. Measurements were performed in a ^{3}He/^{4}He-dilution refrigerator in magnetic fields B up to 16 T. The oscillatory part was deduced by subtracting a polynomial fit from the raw data. The order of polynomial

background was chosen such that its subtraction does not interfere with the lowest frequencies. Oscillation frequencies were determined after Fourier transformation. In order to deduce the angular dependence of the oscillation frequencies the magnetic field was rotated within the crystallographic basal plane and from the (100) direction towards the (001) direction.

Quantum oscillation frequencies are related to the extremal cross-sectional area A of the Fermi surface via the Onsager relation $F = \hbar A/2\pi e$. For simple non-magnetic metals the damping of quantum oscillations is captured by the Lifshitz–Kosevich formula with the damping factors due to impurity scattering [33]

$$R_{\mathrm{D}} = \exp\left(-\frac{B_{\mathrm{D}}}{B}\right) \quad \text{with } B_{\mathrm{D}} = \sqrt{\frac{e\hbar^3 F}{2\pi}}\frac{\kappa p}{k_{\mathrm{B}} l_0} \tag{1}$$

and thermal broadening of the Fermi–Dirac distribution

$$R_{\mathrm{T}} = \frac{X}{\sinh X} \quad \text{with } X = \kappa p \frac{T}{B}\frac{m^\star}{m_{\mathrm{e}}}. \tag{2}$$

Here, $\kappa = 2\pi^2 k_{\mathrm{B}} m_{\mathrm{e}}/e\hbar \approx 14.7\,\mathrm{T\,K^{-1}}$ while p denotes the index of the harmonic, i.e. $p = 1$ for fundamental frequencies. The effect of these two damping factors can be seen in the field and temperature dependence, respectively, of the amplitude of a single frequency. By fitting equations (1) and (2) we extract the mean free path l_0 and the effective mass $m^\star$ of the charge carriers. The large temperature and field range covered in our experiments yield high accuracy determinations of these parameters for the most prominent oscillation frequencies.

3.2. Experimental results

Figure 5 shows a representative trace of the oscillatory part of the resistivity taken at 100 mK for fields between 6 and 16 T with the field applied along the (110) direction. From the Fourier transformed power spectrum, numerous oscillation frequencies are resolved with signal to noise ratios exceeding 100. Note that data in the Fourier spectrum above 13 kT are multiplied by a factor of 10 in order to make the high-frequency peaks more visible. In total, 19 frequencies are detected for this field orientation, some of which are identified as harmonics and some arise from mixing of fundamental frequencies as discussed below. The nomenclature of the frequencies reflects the assignment to orbits on the different Fermi surface sheets, which we deduce from the comparison with band structure calculations below.

The angular dependence of the oscillation frequencies is shown in figure 6 for fields rotated from the (001) direction towards the (100) direction (left panel) and further within the basal plane (right panel). The symmetry observed around 45° in the right panel nicely reflects the crystallographic symmetry around the (110) direction. We observe frequencies from 0.06 to 42.7 kT (for fields along (001)). Generally, more frequencies are observed for fields within the basal plane.

By comparison with our band structure calculation we identify the fundamental frequencies and assign them to extremal orbits of the Fermi surfaces as shown in figure 4. The angular dependence of the predicted frequencies deduced from calculations utilizing $z_{\mathrm{Si}} = 0.379\,c$ are included in figure 6 as solid lines.

For the rotation of the magnetic field from the (001) to the (100) direction the assignment is unambiguous. First, an orbit D1 associated with the hole in the D sheet is predicted which nicely matches the angular dependence of an observed branch. In particular, the angular range over

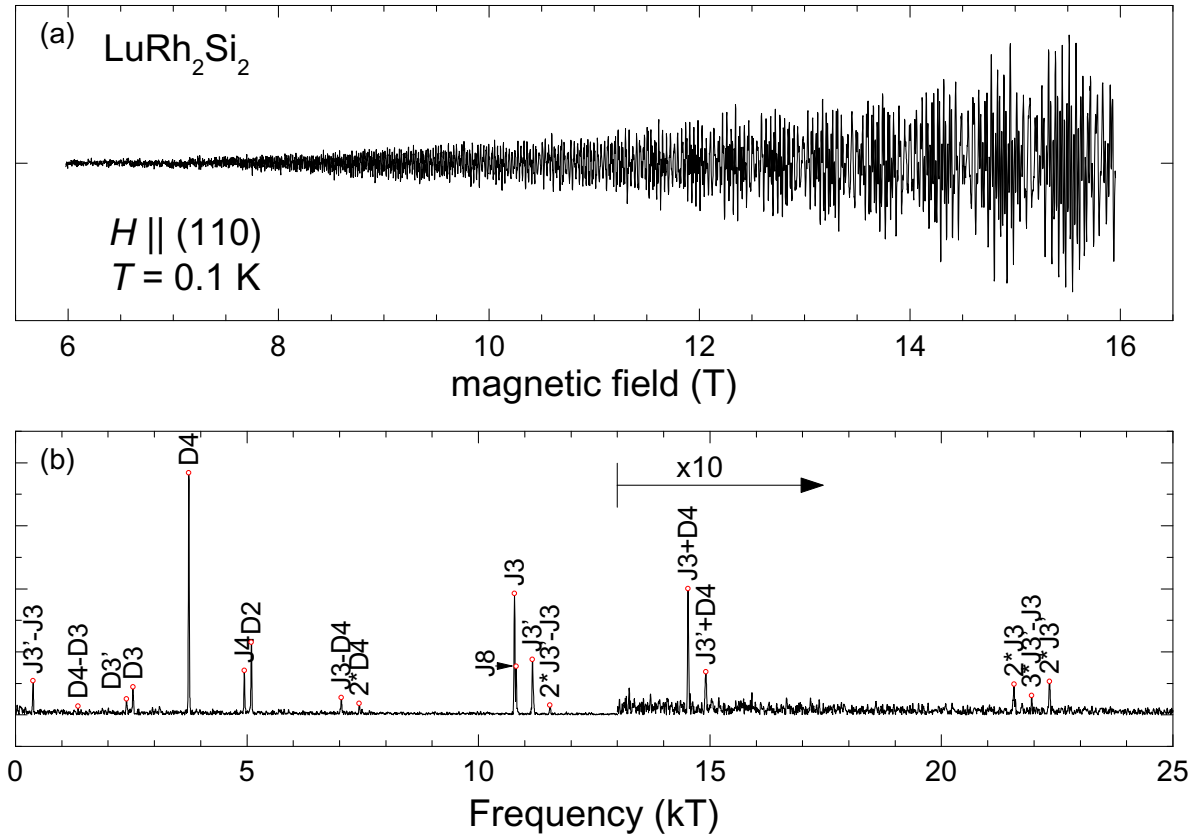

Figure 5. Shubnikov–de Haas oscillations in $LuRh_2Si_2$ [34]. (a) Oscillatory part of the resistivity between 6 and 16 T for field along the (110) direction measured at 100 mK. (b) Fourier transform power spectrum showing quantum oscillation frequencies. Data above 13 kT are magnified by a factor of 10 for better visibility of the high frequency peaks.

which D1 is observed agrees with the predicted angular dependence. The difference between the observed and predicted frequency is very small—note the amplified low frequency scale in the lower part of figure 6. The experimentally determined mass of this orbit agrees very well with the predicted mass as can be seen from tables 2 and 3. In fact, the mass of this orbit strongly supports the usage of $z_{Si} = 0.379\,c$, where our band structure calculations predict a Si p_z character of the states forming this orbit. For smaller z_{Si} the dominating Rh $d_{x^2-y^2}$ band character and flatter dispersion relation yield a significantly larger mass [25]. We also detect the second and third harmonic of the D1 orbit with the mass of the second harmonic very precisely being double of that of the fundamental frequency (the mass of the third harmonic could not be determined due to the strong reduction in intensity).

It is unlikely that the observed frequency corresponds to the pillbox shaped Fermi surface sheet predicted at $z_{Si} \leqslant 0.378$. An outer orbit along the convex shape of the pillbox would lead to a $1/\cos\theta$ form corrected by a small reduction as $\theta \gtrsim 45^\circ$ associated with a rounding of the corners of the pillbox. The experimental data, however, show a small excess with respect to a $1/\cos\theta$ form which is in good agreement with the inner orbit in the convex shaped D sheet. Furthermore, the P sheet has extremal orbits extending all the way to $\theta = 90^\circ$ and also predicts a

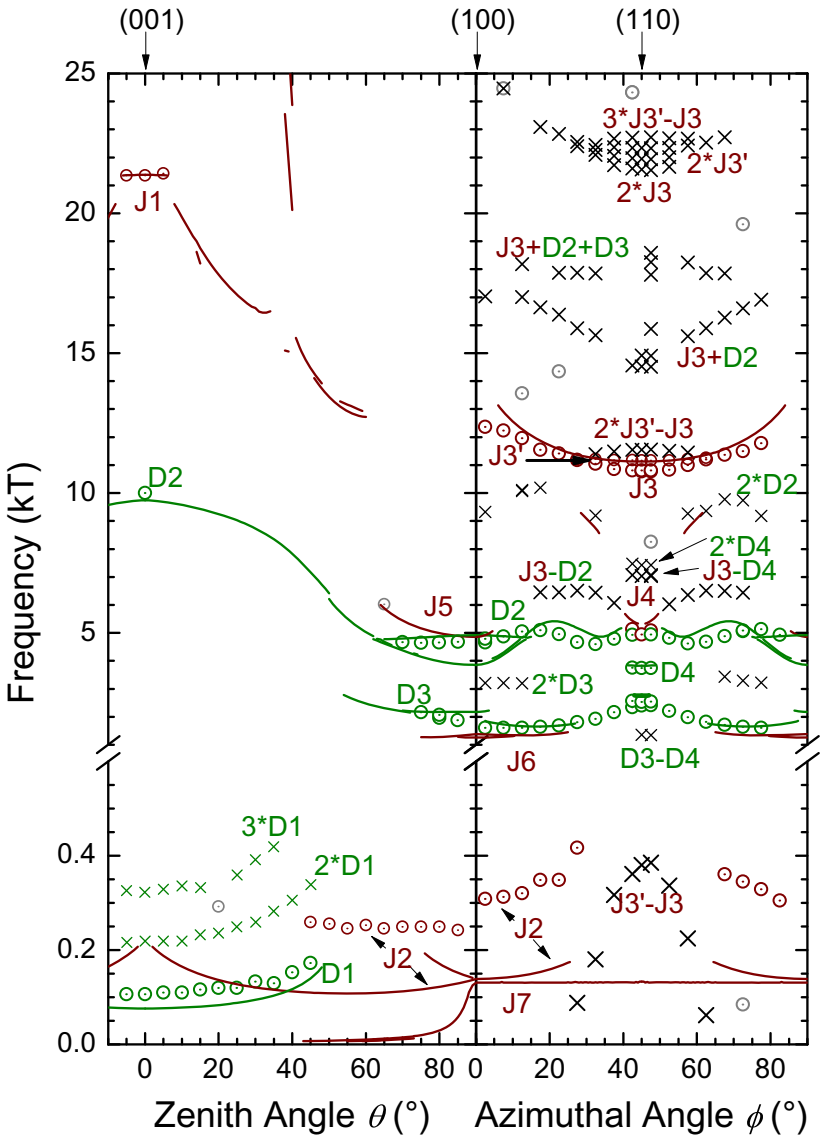

Figure 6. Angular dependence of oscillation frequencies. Data below 0.45 kT are displayed on an expanded scale. No oscillations are observed in the omitted range between 0.45 and 1 kT. Open circles mark fundamental frequencies, whereas crosses correspond to harmonics and frequencies which were identified to arise from mixing of fundamental frequencies (see text for details, section 3.3). Solid lines represent calculated frequencies from our band structure calculations with green and red representing the D and J sheet, respectively, labels refer to the orbits depicted in figure 4. We use the SKEAF code for the extraction of the extremal orbits from our calculated Fermi surfaces [30] (see section 2.1 for details). Top labels and arrows indicate crystallographic orientations.

constant frequency for rotations in the basal plane which is not observed. In general, it is risky to draw conclusions from failure to observe quantum oscillations, particularly since the amplitude of the pillbox orbits is expected to be reduced when the angle differs significantly from the

Table 2. Frequencies and cyclotron masses for field orientations along (110).

	Experimental			Calculated	
Orbit	F(kT)	$m^\star/m_e$	l_0 (μm)	F (kT)	$m^\star/m_e$
J7				0.13	4.3
J3′ − J3	0.38	2.5(4)	0.15(2)		
D3′	2.41	0.7(3)		2.4	0.8[a]
D3	2.54	1.3(5)		2.8	0.4
D4	3.75	0.82(2)	0.32(2)	3.8	0.7
J4	4.95	1.4(5)		5.3	4(2)[b]
D2	5.10	1.17(3)	0.40(5)	5.2	1[c]
J3 − D4	7.05	2.3(1)	0.25(5)		
2 ∗ D4	7.43	1.6(3)			
J3	10.78	1.3(2)[d]	0.4(1)	11.1	1.1
J8	10.81				
J3′	11.17	1.26(2)	0.3–0.6[e]		
2 ∗ J3′ − J3	11.54	3.1(3)	0.38(4)		
J3 + D4	14.53	2.21(7)	0.33(3)		
J3′ + D4	14.91	1.7(2)			
2 ∗ J3	21.57	3.1(3)			
J3′ + J3	21.95	2.4(5)			
2 ∗ J3′	22.33	2.6(2)			

[a] Orbit D3′ only extremal for reduced z_{Si} and at 1° deviation from (110).
[b] Small angular deviation induces large changes in the mass.
[c] Extremal orbit only predicted at 5° deviation from (110) direction.
[d] The mass of $1.3m_e$ was deduced from the analysis of mixed frequencies (see text). The measured mass of $2.29(3)m_e$ is compromised by the J8 frequency which could not be separated in the mass study.
[e] Field dependent mean free path, cf figure 8 and text.

axial direction. However, the fact that we observe a strong signal including the second and third harmonics up to $\theta = 50°$, which suddenly disappears at larger angles, is in contrast to the continuous reduction expected for a pillbox. By contrast, this agrees well with the expectations for the inner orbit in the D sheet, which is not present for angles larger than 50°.

Frequencies detected at 9.99 and 21.35 kT for field along (001) can be assigned to the orbit D2—the circumference of the D sheet—and the orbit J1—the circumference of the J sheet. In both cases we find a good agreement of predicted and experimentally determined effective masses, as can be seen from tables 2 and 3. In addition, we detect the second harmonic of the J1 orbit with its mass in agreement with twice the mass of the fundamental frequency. For the J1 orbit we also see a good agreement with the predicted angular dependence matching very nicely the range over which this orbit is predicted to be extremal. In fact, the predicted range is very small due to the arms of the J sheet interrupting this orbit for larger angles. Consequently, our quantum oscillation results strongly suggest that these arms are present in the J sheet. As for the D1 orbit, it is unlikely that the J1 orbit is lost due to too small a signal at angles $\theta > 5°$, as we observe a very strong signal including the second harmonic, which suddenly vanishes. The D2 frequency, by contrast, has a very small amplitude for magnetic

Table 3. Frequencies and cyclotron masses for field orientations along (001) and (100).

	Experimental		Calculated	
Orbit	F(kT)	$m^\star/m_e$	F(kT)	$m^\star/m_e$
		(001)		
D1	0.11	0.11(5)	0.08	0.11
2 ∗ D1	0.22	0.2(1)		
D2	9.99	2.4(3)	9.7	1.9
J1	21.35	1.54(2)	21.4	1.3
2 ∗ J1	42.73	2.5(5)		
		(100)		
J7			0.13	4.3
J2	0.25	1.3(5)[a]	0.14	0.5[a]
J6			1.26	1.8
J6′			1.38	2.6
D3	1.61	0.5(1)[b]	1.8	0.56[b]
D3	1.81	0.4(3)[a]	2.2	0.5[a]
2 ∗ D3	3.22	1.2(4)		
D2	4.64	0.8(1)[a]	4.9	0.6[a]
D2	4.64	1.1(1)[b]	4.9	0.6[b]
D2	4.74	1.1(1)[b]		
J3	12.36	2.43(2)[b]	12.7	3[b,c]

[a] ≈5° off towards (001).
[b] ≈3° off towards (110).
[c] Extremal orbit only predicted at 5° towards (110) direction.

field parallel to (001) and may very well be lost due to further reduction as the field is rotated away from this direction.

As the field direction approaches the basal plane, the D2 orbit is detected again at a frequency of 4.7 kT for $\theta \geqslant 70^\circ$, nicely reproducing the flat angular dependence of one branch associated with this orbit as well as the mass expected for the (100) direction (cf tables 2 and 3). The two branches correspond to different extremal orbits, as depicted in figure 4. This orbit is also observed for rotation in the basal plane with a good match to the predicted angular dependence. Only in close vicinity of the (110) direction of magnetic field is this orbit not expected to persist. However, for angles $42.5^\circ \leqslant \phi \leqslant 45^\circ$ two frequencies 4.9 and 5.1 kT are observed. One of these may be associated with the J4 orbit of the J sheet while the other one might still arise for the D2 orbit due to small misalignment. In fact, the mass predicted for the D2 orbit at a small angle nicely matches the observed mass of the 5.1 kT oscillations (cf tables 2 and 3). The mass of the J4 orbit is expected to be much larger than observed for the 4.9 kT frequency, however again, small misalignments yield an improved agreement.

A frequency of about 1.6 kT is observed close to the (100) direction which is assigned to an orbit D3 circling from the hole to the circumference of the D sheet (cf figure 4). Both the

angular dependence and the mass agrees well with the results of the band structure calculations (cf tables 2 and 3) for field orientations out of the basal plane and along the (100) direction. For intermediate angles in the basal plane $30^\circ \leqslant \phi \leqslant 40^\circ$ this orbit is expected to be non-extremal. It might be that we observe oscillations associated with a non-extremal orbit. This is in agreement with the fact that the amplitude of this frequency is strongly reduced to almost noise level in this angular range while other frequencies preserve a strong amplitude. However, small misalignments in the experiment or approximations in the band structure calculations can result in an extremal orbit. It would require further experimental and computational work to scrutinize the hypothesis of a non-extremal orbit.

For angles close to the (110) direction $40^\circ \leqslant \phi \leqslant 45^\circ$, two frequencies D3 and D3′ are observed. Both have almost no angular dependence, in agreement with an extremal orbit D3 present over a very limited angular range $43^\circ \leqslant \phi \leqslant 45^\circ$. The mass of this orbit agrees within experimental accuracy with the lower frequency D3′. For small misalignments ($\approx 1^\circ$) and slightly reduced z_{Si} our band structure calculations predict two orbits D3 and D3′ with frequencies 2.4 and 2.8 kT close by. Their predicted masses of $0.8m_{\mathrm{e}}$ and $0.4m_{\mathrm{e}}$ are in reasonable agreement given the large uncertainty of the measured mass for D3. This supports the above suggestion of corrections to the band structure calculations to improve agreement with experimental results.

The frequency with the largest amplitude in the power spectrum at 3.7 kT (cf figure 5) is observed in a small angular range of 2.5° around the (110) direction only. This nicely matches the predicted range for the D4 orbit of the D sheet with also the predicted mass in good agreement with the observed value (cf tables 2 and 3). This orbit is very sensitive to changes in the Si position z_{Si} in our band structure calculations and vanishes for $z_{\mathrm{Si}} > 0.380\,c$ giving a strong upper boundary for z_{Si}.

A frequency with small angular dependence around 0.25 kT is observed in the rotation study from (001) to (100) in the range $45^\circ \leqslant \theta \leqslant 90^\circ$. This frequency is slightly larger than that expected for the J2 orbit circling on the outside of the arms in the J sheet but roughly matches its angular dependence. In addition, this orbit is predicted to continue for rotations in the basal plane up to $\phi \leqslant 25^\circ$ with a significant increase of frequency as ϕ increases. This nicely matches the continued branch observed (the small offset of 0.05 kT from rotation out of the basal plane to that in the basal plane may be due to a small misalignment of the sample in the two subsequent rotation studies).

A group of strong frequencies is found around 11 kT for fields along the (110) direction. The lowest of these frequencies (10.8 kT) has the largest amplitude in the power spectrum (cf figure 5) and can be traced over the complete range of our rotation study towards the (100) direction down to $\phi \geqslant 2.5^\circ$. A high resolution study of this frequency over a wide field range reveals a two peak structure (cf figure 5) with 10.78 and 10.81 kT. The higher amplitude arises from the lower frequency, i.e. 10.78 kT. The angular dependence of this frequency shows good agreement with the predicted angular dependence of the J3 orbit circling the inside of the main body of the J sheet. It is natural to assign the frequency at 10.78 kT with largest amplitude to the J3 orbit. We surmise that the frequency of 10.81 kT with the lower amplitude is a secondary effect and label this frequency J8 although we have no proof for it to be related to the J sheet.

The fact that J3 is detected almost all the way to the (100) direction indicates that the arms of the J sheet are very small as these interrupt the J3 orbit for fields along (100). In fact, for smaller z_{Si} the band structure calculations predict the angular range of the J3 orbit to narrow very rapidly, thus, the observed angular dependence of the J3 orbit strongly supports

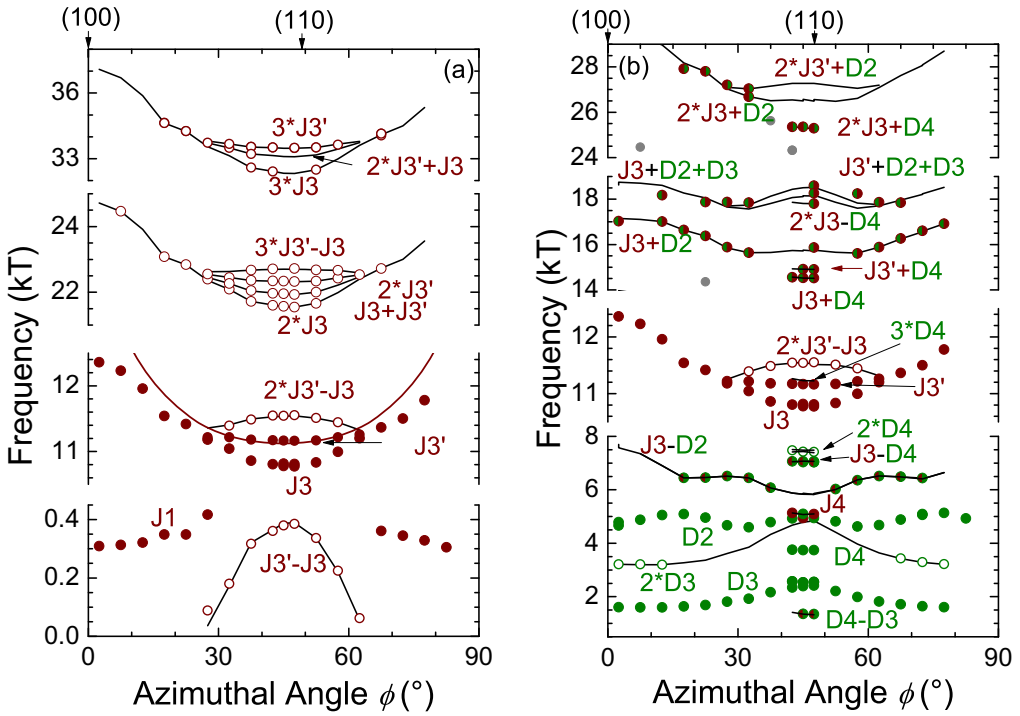

Figure 7. Frequency mixing was identified with the help of an algorithm comparing all measured frequencies against all combinations of sums and differences of observed frequencies. Fundamental frequencies were deduced from the comparison with band structure calculations. Symbols mark detected frequencies, solid black lines mark frequencies calculated from sums and differences of fundamental frequencies as indicated by the labels. Panel (a) depicts the mixing of the J3 orbit with the J3′ orbit and harmonics while (b) depicts the mixing and harmonics of the J3 and J3′ orbit with orbits of the D-sheet, i.e. D2, D3 and D4. The solid red line in (a) reproduces the calculated angular dependence of the J3 orbit from figure 6.

the experimental value for z_{Si}. The frequencies at 11.2 and 11.5 kT have a smaller amplitude and are limited in the angular range to $27.5^\circ \leqslant \phi \leqslant 45^\circ$. The frequencies around 11 kT give rise to various harmonics and mixed frequencies. From the detailed analysis we identify one of the 10.8 kT frequencies and the 11.2 kT frequency to be the fundamental frequencies. We dub them J3 and J3′ as both bear resemblance with the angular dependence and masses expected for the J3 orbit. In the following we argue that one of them is the fundamental frequency; however, the mechanism yielding the second frequency remains elusive.

3.3. Frequency mixing analysis

The measured frequencies are presented in figure 7(a) together with the calculated harmonics and mixed frequencies of J3 and J3′. Clearly, we detect second and third harmonics of both J3 and J3′. We also detect the sum and difference of these two frequencies, i.e. J3 ± J3′. In addition, we detect the sum and difference of twice J3′ with J3, i.e. $2 * \mathrm{J3}' \pm \mathrm{J3}$. Finally, we also detect

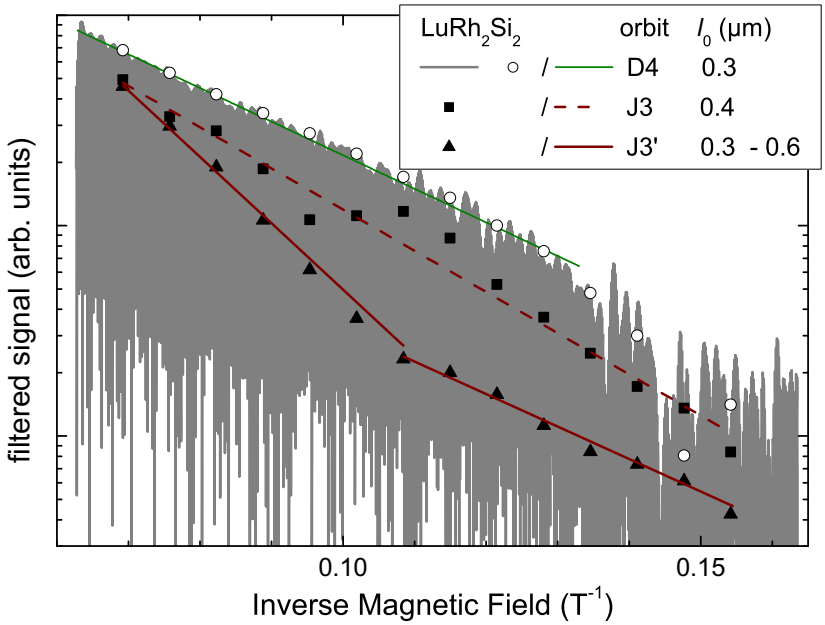

Figure 8. Dingle analysis of the field dependent amplitude [33] for the frequencies D4, J3 and J3′. The mean free path was extracted by fitting equation (1) to the maxima of the oscillations for D4 whereas for all other frequencies a moving window Fourier transform was used to extract a field dependent amplitude (squares and triangles). Cross-checking the two methods for the D4 orbit yielded good agreement as shown by the grey curve and open circles. For the J3′ orbit (triangles) different values of the mean free path were found below and above 9 T as can be seen by the two fits with distinct slope (red solid lines).

the difference of $3 * \mathrm{J3}' - \mathrm{J3}$. The analogous sum $3 * \mathrm{J3}' + \mathrm{J3}$ was not detected, possibly because of unfavourable sampling for such high frequencies.

Possible mechanisms for frequency mixing are magnetic breakdown and magnetic interaction. The former arises when the magnetic field exceeds the equivalent energy gap separating orbits close by in k-space [33]. The latter arises because the sample's magnetization—which itself oscillates with varying field—feeds back into the magnetic induction field B.

The pattern of frequencies, i.e. the observation of sums and differences, is most consistent with magnetic interaction of two fundamental frequencies J3 and J3′. In particular, considering first and second order effects, i.e. including fundamental frequencies J3 and J3′ and second harmonics $2 * \mathrm{J3}$ and $2 * \mathrm{J3}'$ in the oscillating magnetization yields the observed second and third harmonics as well as the sums and differences of the fundamental and harmonic frequencies.

Magnetic breakdown can be identified by a characteristic variation of the oscillation amplitude with field: the amplitude of the fundamental frequency is expected to be reduced above the breakdown field whereas the sums and differences are expected to be present above the breakdown field only. We do observe unperturbed damping of the J3 and D4 orbit as can be seen from figure 8. The damping of the J3′ orbit shows some irregularities which we discuss below but the damping is inconsistent with a reduction of this frequency above the breakdown

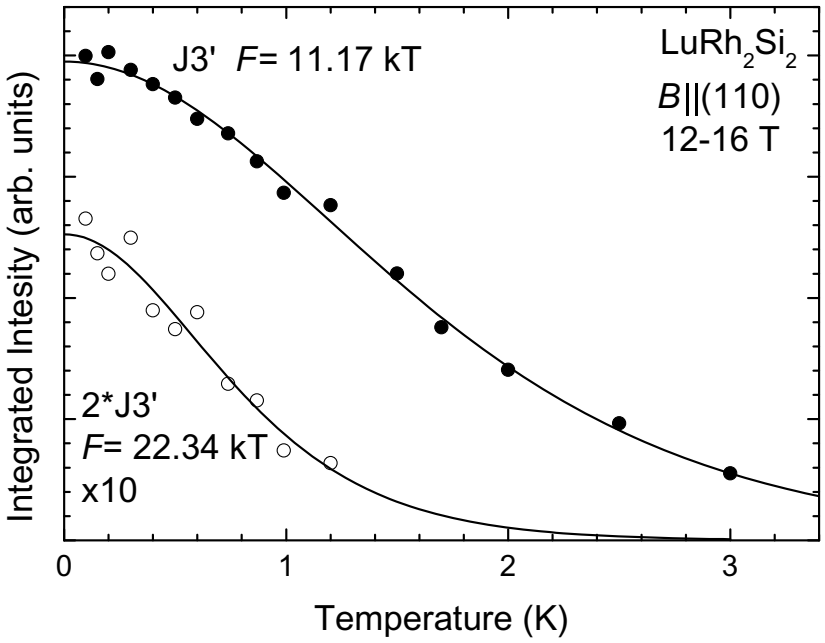

Figure 9. Lifshitz–Kosevich analysis of the temperature dependent amplitude for the J3′ frequency and its harmonic $2 * J3'$. For the latter the amplitude is enlarged by a factor of 10 for better visualization. The effective mass was deduced by fitting equation (2).

field. In summary, this suggests that magnetic interaction is the origin for the mixing of the J3 and J3′ frequency.

The masses for second harmonics are expected to be twice that of the fundamental and for the difference and sum the mass is expected to be the sum of the individual masses. This is not immediately consistent with the experimentally observed masses. However, we have to take into account that J3 and J8 could not be separated in the mass study. Therefore, the directly measured mass of the J3 and J8 frequency may not reflect the mass of the J3 orbit. Analysing the harmonics and mixed frequencies we are able to reconstruct the mass of J3. The second harmonic of J3′ has twice the mass of J3′ (cf figure 9 and tables 2 and 3). For the sum and difference $J3' \pm J3$ we measure almost identical masses like for the second harmonic of J3′. Consequently, this suggests that J3 has the same mass as J3′, i.e. $1.3m_e$. We note that the harmonic of J3 has a mass inconsistent with twice its fundamental mass which might be due to the influence of the non-separable frequencies J3 and J8 contributing in different ratios to the fundamental and harmonic frequency.

A mass of $1.3m_e$ for the J3 orbit is highly consistent with the mixing of this frequency with other orbits. We find mixing of J3 with D4, D3 and D2 as can be seen from the detailed analysis in figure 7(b). In the case of the sum and difference with D4, i.e. $J3 \pm D4$ we measure similar masses of $2.2m_e$ and $2.3m_e$ which is close to the sum of the individual masses $1.3m_e + 0.8m_e = 2.1m_e$. We note that the angular dependence of the frequency identified with $2 * D4$ is also compatible with $J3' - D4$ (two solid black lines close by in the bottom panel of figure 7(b)); the mass of this frequency however, is twice that of D4 rather than the sum of the masses of J3′ and D4. Consequently, we identify this frequency with the harmonic of the D4

orbit. This implies that the third harmonic $3*$D4 is very close to J3′. However, $3*$D4 cannot account for the J3′ orbit as D4 is limited to a much narrower angular range and $3*$D4 is also slightly higher in frequency (cf second panel from bottom in figure 7(b)).

We can rule out magnetic breakdown to yield the observed frequencies J3 ± D4 as the orbits of J3 and D4 are well separated in k-space (cf figure 4). This is in line with the earlier conclusion that also J3 and J3′ mix via magnetic interaction.

It remains unclear why we observe two frequencies J3 and J3′ rather than only one. One is certainly the J3 orbit on the J sheet. The other one, however, is not predicted by the band structure calculations. The absolute value of the predicted frequency matches best with J3′. However, the angular dependence favours the lower frequency with a small offset. As this is also the frequency with the higher amplitude we assign the 10.78 kT frequency with the J3 orbit.

We can rule out twinning and crystal domains to give rise to the two frequencies J3 and J3′ as this is in contradiction with the merging of the two at $\phi \approx 30^\circ$. If two domains were aligned along the c-direction but misaligned in the basal plane this would yield a continuously shrinking difference of the two frequencies for $\phi \to 0^\circ$.

For magnetic breakdown one expects deviations of the field dependence of the amplitude from the Dingle behaviour described by equation (1). Indeed, we find anomalies in the Dingle analysis of J3′. This is illustrated in figure 8. Two distinct slopes are present for J3′ in the logarithmic representation against $1/B$. This is in contrast to all other frequencies that are strong enough and separable for a Dingle analysis; and which show a single slope over the full range investigated. The change of slope for J3′ is showing an increased amplitude above 9 T. The small deviations of J3 from exponential damping (linear behaviour in figure 8) around 10 T are most likely due to the presence of the secondary peak at this frequency that also shows up as a perturbation in the mass analysis. In particular, the slope at very high and small fields are identical, in contrast to the behaviour expected for magnetic breakdown.

The enhanced amplitude of J3′ above 9 T may originate from magnetic breakdown yielding the J3′ frequency, although it remains unclear which orbits are involved. The orbit J7 associated with the pillar in the J sheet is one possibility. An orbit around the pillbox of the P band might come into play when the spin majority branch starts to populate in high magnetic fields. For both cases, however, an isotropic behaviour would be expected for rotations in the basal plane in contrast to the vanishing splitting between J3 and J3′ in the rotation towards (100), $\phi \to 0^\circ$. Interestingly, if magnetic breakdown proves to be the origin of J3′ this allows one to study the combination of magnetic breakdown yielding J3′ and magnetic interaction of J3 and J3′ in $LuRh_2Si_2$.

4. Discussion

4.1. Comparison to $YbRh_2Si_2$

Our electronic structure studies on $LuRh_2Si_2$ provide important refinement relevant for understanding $YbRh_2Si_2$. First, we find that $z_{Si} = 0.379\,c$ should be used for accurate band structure calculations. Here, we present refined LDA band structure calculations on $YbRh_2Si_2$. The sensitivity to z_{Si} mostly affects calculations of the 'small' Fermi surface configuration in which the f electrons were treated as core electrons not hybridizing with the conduction electrons. This configuration parallels the natural configuration of $LuRh_2Si_2$ for which the

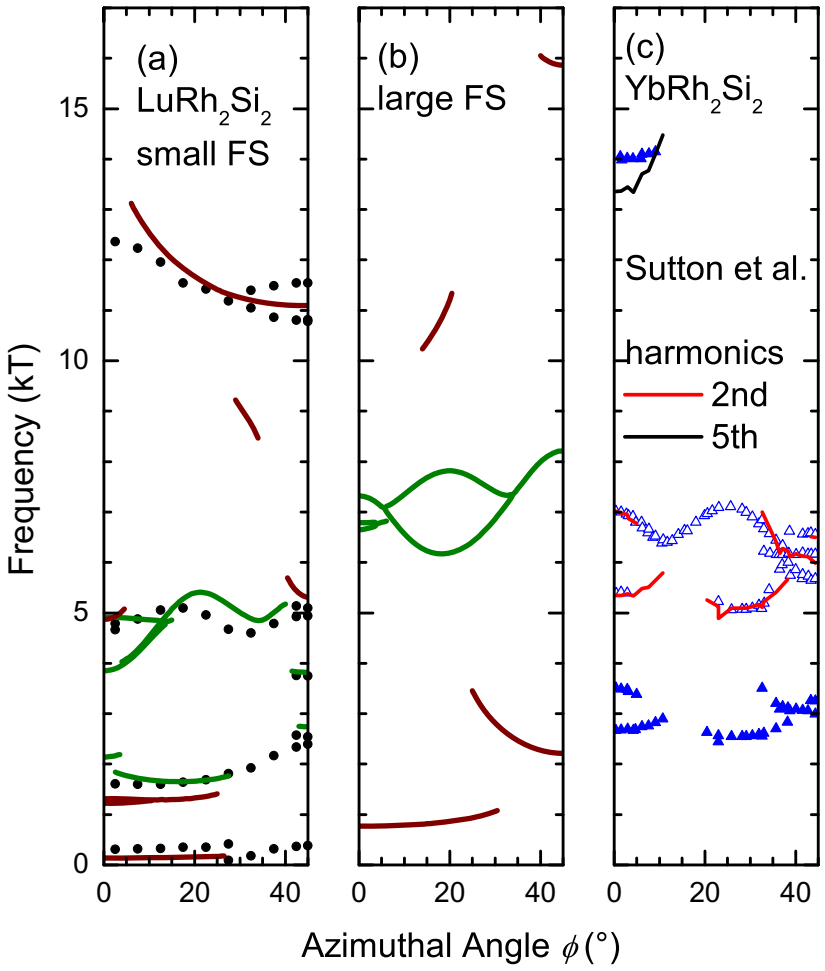

Figure 10. Comparison of quantum oscillation measurements on $LuRh_2Si_2$ (a) and $YbRh_2Si_2$ (c) [18] with band structure calculations of $YbRh_2Si_2$ treating the f states as core electrons ('small' Fermi surface, (a)) and as fully itinerant ('large' Fermi surface, (b)). Red and black lines in (c) denote second and fifth harmonics of the fundamental frequencies below 4 kT. Open symbols mark the frequencies possibly originating from harmonics.

f electrons form a completely filled shell. LDA calculations of this configuration were used in [15, 18, 20] for comparison with quantum oscillation measurements. The high frequency of 14 kT reported in [18] for fields along the (100) direction has been assigned to an orbit of the J-sheet of the 'small' Fermi surface configuration. In general this frequency cannot be mapped to any of the orbits on the D-sheet as these are limited to below 8 kT in both the 'small' and 'large' Fermi surface calculation. Nevertheless the assignment with a branch predicted for the 'small' Fermi surface calculation needs to be revised in the light of our results on $LuRh_2Si_2$.

In figure 10 we present a comparison of refined band structure calculations on $YbRh_2Si_2$ with the quantum oscillation measurements of [18]. We adopt identical parameters as used in [18] except for the refined lattice parameters (cf table 1). Since slight variations of c originate in minute variations of the Rh content [12], we employ an average value of $c = 9.86$ Å

Table 4. Frequencies and masses expected for second harmonics of the frequencies below 4 kT compared to measured frequencies and masses between 5 and 7 kT in $YbRh_2Si_2$ after [18].

Second harmonic of frequencies below 4 kT		Detected frequencies between 5 and 7 kT	
$2 * F$	$2 * m^\star/m_e$	F	$m^\star/m_e$
5.3	23	5.37	9.2
7.0	12	7.01	12.3
6.4	14	6.54	13.2

for our calculations on $YbRh_2Si_2$. In the case of the 'small' Fermi surface configuration (simulated by calculating $LuRh_2Si_2$ utilizing crystal lattice parameters of $YbRh_2Si_2$) we find virtually no difference to the results using lattice parameters of $LuRh_2Si_2$ (cf figure 6). Consequently, the Shubnikov–de Haas measurements on $LuRh_2Si_2$ complemented by the band structure calculations can directly be used as a 'small' Fermi surface reference of $YbRh_2Si_2$. Importantly, within this 'small' Fermi surface calculation of $YbRh_2Si_2$ no high-frequency orbit is predicted for field along (100). The J3 orbit is observed in the Shubnikov–de Haas measurements on $LuRh_2Si_2$ all the way to (100), but has an opposing angular dependence compared to the branch observed in $YbRh_2Si_2$. This indicates that the 14 kT frequency reported in [18] may not be assigned to the 'small' Fermi surface configuration.

Likewise, the 'large' Fermi surface calculations as simulated in [15, 18] with fully itinerant LDA calculations of $YbRh_2Si_2$ are sensitively affected by the choice of z_{Si}. Using the refined lattice parameters listed in table 1 we find some major changes as can be seen from figure 10. A central hole emerges in the J sheet, which limits extremal orbits encircling the sheet to angles between 15° and 20°—this limits the 11 kT frequency to a narrow angular range (cf figure 10(b)). A new extremal orbit through this central hole arises for angles above 40°, which extends beyond the boundary of the first Brillouin zone and has a high frequency of 16 kT.

The low frequency branches and the extremal orbits of the D-sheet are not affected by the change of the experimental lattice parameters. The orbits on the D-sheet (green lines in figure 10(a)) were earlier identified with all orbits observed in $YbRh_2Si_2$ below 7 kT. In the light of the extensive presence of harmonics in $LuRh_2Si_2$ we re-examine the data on $YbRh_2Si_2$. We include second and fifth harmonics of the frequencies below 4 kT as red and black solid lines, respectively, in figure 10(c). The frequencies between 5 and 7 kT very well match the angular dependence of the second harmonic. This matching extends also for rotations towards the (001) direction reported in [15]. For two of the three putative harmonics the masses reported in [18] show the expected scaling (cf equation (2)), as summarized in table 4. The fifth harmonic (black line in figure 10), however, does not match with the observed branch at 14 kT suggesting this branch to be a fundamental frequency. This is in line with the expected reduction of intensity for high harmonics.

As indicated above harmonics are in general suppressed [33]. This seems to contradict the suggested assignment of the frequencies between 5 and 7 kT to second harmonics as they are observed over a wider angular range with larger intensity than the proposed fundamental frequencies below 4 kT. However, there are two mechanisms which can compensate for this

reduction: (i) magnetic interaction can lead to an enhanced amplitude. (ii) The modulation technique used for the de Haas–van Alphen measurements on $YbRh_2Si_2$ in [15, 18] favours the detection of higher frequencies and harmonics; for a typical modulation field of 10 mT the Bessel function determining the amplitude of the quantum oscillations in the field modulation technique yields a damping factor of ≈4 for the frequencies below 4 kT with respect to those between 5 and 7 kT. An enhanced second harmonic has been observed in $CeRhIn_5$ [35].

In [15] it was suggested that the frequencies below and between 5 and 7 kT arise from orbits through the central hole of the D sheet and slightly off-centre orbits spanning the full cross-section, respectively. In principle, this can yield roughly a factor of 2 between the two groups of frequencies. However, the precise matching of the angular dependence of the putative harmonic apparent in figure 10(c) gives a very low upper boundary for the hole in the D sheet as it would otherwise violate the matching of the high frequencies with the second harmonics. In addition, the scaling should break down for rotations towards the *c*-direction. An earlier de Haas–van Alphen study covered a range up to 60° out of plane over which the frequencies seem to fit with the scaling whereas the masses do deviate from the expected scaling [15]. In order to distinguish between the two possibilities we suggest quantum oscillation measurements extending the angular range all the way to *c*-axis. Here, the de Haas–van Alphen measurement of the susceptibility is unfavourable as the susceptibility is strongly reduced for this direction. This magnetic anisotropy, however, is favourable for quantum oscillation measurements using torque magnetometry. Alternatively, Shubnikov–de Haas may allow one to follow the quantum oscillations to the *c*-axis orientation.

If the frequencies between 5 and 7 kT prove to be truly harmonics this reduces the basis for comparison with band structure calculations to the observed frequencies below 4 kT and above 14 kT, which are not matched by a harmonic of the low frequencies (cf black line in figure 10(c)).

Overall, the agreement of the data on $YbRh_2Si_2$ with the LDA calculations of both the 'small' and 'large' Fermi surface is rather limited, particularly with the branches between 5 and 7 kT possibly arising from harmonics and thus not available for comparison with band structure calculations. The remaining fundamental frequencies below 4 kT have neither a good agreement with the 'small' nor the 'large' Fermi surface calculation. Likewise the high frequency of ≈14 kT, which appears to be a fundamental frequency, cannot be mapped to orbits of the LDA calculations, yet due to the fact that the largest orbits on the D-sheet are well below 9 kT this frequency very likely originates from the J-sheet. LDA is very well capable to predict the Fermi surface and expected quantum oscillation frequencies of normal metals, and we demonstrate the qualitative and quantitative agreement for $LuRh_2Si_2$. The 'small' Fermi surface configuration of $YbRh_2Si_2$ with conduction electrons decoupled from the f electrons is expected to be such a normal metal. For Yb-based heavy fermion materials with interacting conduction and f electrons, however, LDA is known to fall short in predicting the Fermi surface topology and quasiparticle masses [19, 23, 36]. Consequently, the discrepancy of our refined calculations of the 'small' Fermi surface with earlier de Haas–van Alphen measurements on $YbRh_2Si_2$ precludes the 'small' Fermi surface configuration and supports the relevance of the f electrons in the high-field regime. While the discrepancy with the LDA band structure calculations of the 'large' Fermi surface is expected, they reinforce the need for more sophisticated models like a renormalized band approach [37] or dynamical mean field theory [38, 39] to accurately predict the electronic structure of $YbRh_2Si_2$ and to match the observed angular dependence of quantum oscillation frequencies.

4.2. Two-band character in Hall effect of $LuRh_2Si_2$

In Hall effect measurements on $LuRh_2Si_2$ a pronounced crossover of the Hall coefficient as a function of temperature was found [4]. Through comparison with band structure calculations this could be attributed to a crossover between regimes with different relative scattering rates for the two dominating bands. The analysis in terms of a two-band model revealed similar scattering rates for the two bands at low temperatures, while they differ significantly at high temperatures. In our Shubnikov–de Haas measurements we were able to extract the mean free path for the different orbits at low temperature, as illustrated in figure 8. We find that the mean free paths extracted for different fundamental orbits to differ by 20%. The J3′ orbit shows deviations at high fields (exceeding the field scale of the Hall effect measurements). This agrees well with the result obtained through the two-band analysis.

While the two-band model gives a very convincing qualitative description of the Hall effect, including the temperature range of the crossover, a small quantitative difference remains at high temperatures which could only be resolved assuming slightly different values for the Hall coefficients of the two major bands compared to the outcome of previous band structure calculations [4]. The previous electronic structure calculations were based on a generic $z_{Si} = 0.375\,c$. Our refined band structure calculations might correct for this small difference.

We note that the magnetic breakdown possibly contributing to the mixing of the various frequencies cannot account for the change in slope of the Hall resistivity [40]. The Hall measurements were conducted with fields along the (001) direction whereas frequency mixing is seen for fields in the basal plane only. Also, the crossover in mean free path observed for the J3′ orbit is observed for fields along the (110) direction and at much higher fields than the crossover in Hall effect [4, 40].

Likewise it is unlikely that a thermally excited population of the P sheet at temperatures of the order of 100 K can account for the change in Hall coefficient as a function of temperature. The charge carrier concentration of this band will be very small compared to the other bands and its effect is therefore negligible.

5. Conclusion

We present a comprehensive study of the electronic structure of $LuRh_2Si_2$ which—owing to almost identical lattice parameters—serves as an ideal non-magnetic reference for the intensively studied heavy-fermion material $YbRh_2Si_2$. We find a sensitive dependence of the Fermi surface topology on the position of the Si atoms z_{Si}. Best agreement between predicted and measured quantum oscillation frequencies is obtained at the experimental value $z_{Si} = 0.379\,c$, very close to the value $0.381\,c$ obtained from lattice relaxation. We therefore recommend usage of the precisely determined experimental lattice parameters for future band structure calculations on $LuRh_2Si_2$ and $YbRh_2Si_2$. Moreover, these findings establish the universality of the sensitivity in electronic properties to the Wyckoff z parameter in the $ThCr_2Si_2$ structure shared by many prominent compounds, including the iron pnictide superconductors which feature an even wider variation of z [26].

The re-examination of de Haas–van Alphen measurements on $YbRh_2Si_2$ suggests previously unidentified harmonics which reduce the number of fundamental frequencies to a group of frequencies below 4 kT and a single frequency at 14 kT. We compare these frequencies with both the results on $LuRh_2Si_2$ and LDA calculations, which are consistently capable of

describing the 'small' Fermi surface configuration within the f-core treatment. This comparison reveals strong deviation which support the conclusion that the $YbRh_2Si_2$ f electrons do not localize at $\mu_0 H_0 \approx 10$T.

Acknowledgments

The authors thank Gil Lonzarich and Stephen Julian for fruitful discussions. We thank Yuri Grin for crystal structure refinement and Lina Klintberg and Cornelius Krellner for technical support. SF acknowledges support by the Alexander von Humboldt foundation, ERC and Darwin College Cambridge. PR acknowledges support by the Cusanuswerk and the EPSRC. SKG acknowledges support by Trinity College, Cambridge. MLS was supported by the Royal Society. This work was partially supported by NSF-DMR-0710492 and NSF-PHY-0551164, FP7-ERC-227378.

References

[1] Kimber S A J *et al* 2009 *Nature Mater.* **8** 471–5
[2] Steglich F, Aarts J, Bredl C D, Lieke W, Meschede D, Franz W and Schäfer H 1979 *Phys. Rev. Lett.* **43** 1892
[3] Oeschler N, Hartmann S, Pikul A P, Krellner C, Geibel C and Steglich F 2008 *Physica* B **403** 1254–6
[4] Friedemann S *et al* 2010 *Phys. Rev.* B **82** 35103
[5] Gegenwart P *et al* 2002 *Phys. Rev. Lett.* **89** 56402
[6] Si Q, Rabello S, Ingersent K and Smith J L 2001 *Nature* **413** 804–8
[7] Paschen S *et al* 2004 *Nature* **432** 881–5
[8] Friedemann S *et al* 2010 *Proc. Natl Acad. Sci. USA* **107** 14547–51
[9] Friedemann S *et al* 2009 *Nature Phys.* **5** 465–9
[10] Caroca-Canales N 2010 private communication
[11] Cardoso R 2011 private communication
[12] Wirth S *et al* 2012 *J. Phys.: Condens. Matter* **24** 294203
[13] Dionicio G A 2006 Electrical resistivity of $YbRh_2Si_2$ and EuT_2Ge_2 (T = Co, Cu) at extreme conditions of pressure and temperature *PhD Thesis* Technischen Universität Dresden
[14] Pfau H *et al* 2013 *Phys. Rev. Lett.* **110** 256403
[15] Rourke P M C, McCollam A, Lapertot G, Knebel G, Flouquet J and Julian S R 2008 *Phys. Rev. Lett.* **101** 237205
[16] Gegenwart P *et al* 2006 *New J. Phys.* **8** 171
[17] Zwicknagl G 2011 *J. Phys.: Condens. Matter* **23** 94215
[18] Sutton A B *et al* 2010 *Phys. Status Solidi* b **247** 549–52
[19] Herbst J F and Wilkins J W 1984 *Phys. Rev.* B **29** 5992–4
[20] Knebel G *et al* 2006 *J. Phys. Soc. Japan* **75** 114709
[21] Suzuki M-T and Harima H 2010 *J. Phys. Soc. Japan* **79** 024705
[22] Lee C-H *et al* 2008 *J. Phys. Soc. Japan* **77** 083704
[23] Wigger G A, Baumberger F, Shen Z-X, Yin Z P, Pickett W E, Maquilon S and Fisk Z 2007 *Phys. Rev.* B **76** 35106
[24] Jeong T 2006 *J. Phys.: Condens. Matter* **18** 10529
[25] Reiss P, Rourke P M C, Zwicknagl G, Grosche F M and Friedemann S 2013 *Phys. Status Solidi* b **250** 498–501
[26] Johnston D C 2010 *Adv. Phys.* **59** 803–1061
[27] Blaha P, Schwarz K, Madsen G K H, Kvasnicka D and Luitz J 2001 *WIEN2k, An Augmented Plane Wave + Local Orbitals Program for Calculating Crystal Properties* www.wien2k.at/
[28] Perdew J P, Burke K and Ernzerhof M 1996 *Phys. Rev. Lett.* **77** 3865–8

[29] Kokalj A 1999 *J. Mol. Graph. Model.* **17** 176–9
[30] Rourke P M C and Julian S R 2012 *Comput. Phys. Commun.* **183** 324–32
[31] Rourke P M C, McCollam A, Lapertot G, Knebel G, Flouquet J and Julian S R 2009 *J. Phys.: Conf. Ser.* **150** 042165
[32] MaQuilon S 2007 The non-fermi liquid effects in the heavy fermion kondo systems of $Lu_{1-x}Yb_xM_2Si_2$ M = Rh, Cu *PhD Thesis* UC Davis
[33] Shoenberg D 2009 *Magnetic Oscillations in Metals* (Cambridge: Cambridge University Press)
[34] Friedemann S, Goh S K, Grosche F M, Fisk Z and Sutherland M 2012 *J. Phys.: Conf. Ser.* **391** 012011
[35] Shishido H, Settai R, Harima H and Onuki Y 2005 *J. Phys. Soc. Japan* **74** 1103–6
[36] Norman M R 2005 *Phys. Rev.* B **71** 220405
[37] Zwicknagl G 1992 *Adv. Phys.* **41** 203–302
[38] Georges A, Kotliar G, Krauth W and Rozenberg M J 1996 *Rev. Mod. Phys.* **68** 13–25
[39] Kotliar G, Savrasov S Y, Haule K, Oudovenko V S, Parcollet O and Marianetti C A 2006 *Rev. Mod. Phys.* **78** 865–951
[40] Friedemann S, Oeschler N, Wirth S, Steglich F, MaQuilon S and Fisk Z 2010 *Phys. Status Solidi* b **247** 723–6